PAPER

The single-band red upconversion luminescence from morphology and size controllable Er^{3+}/Yb^{3+} doped MnF_2 nanostructures†

Zhenhua Bai,[a] Hui Lin,[b] Jesse Johnson,[a] Sa Chu Rong Gui,[b] Kenji Imakita,[b] Reza Montazami,[a] Minoru Fujii[b] and Nastaran Hashemi*[a]

Er^{3+}/Yb^{3+} doped MnF_2 nanostructures have been prepared *via* a solvothermal method. The morphology of the nanocrystals could be well controlled from nanoparticles to nanoclusters and nanolanterns by varying the volume ratio between oleic acid and ethanol in the solvent. Moreover, the size is tuned from 200 nm to 1.5 μm with the increase of reaction temperature from 110 to 200 °C. It is shown that controlling the doping concentration ($Yb^{3+} \leq 20$ mol%) is essential to preserve the single phase and morphology of the MnF_2 host. Single-band red upconversion (UC) emission can be generated in Er^{3+} single and Er^{3+}/Yb^{3+} codoped MnF_2 nanoclusters due to the energy transfer between host Mn^{2+} and dopant Er^{3+} ions. The detailed studies suggest that our $MnF_2:Er^{3+}/Yb^{3+}$ nanocrystals have the strongest single-band luminescence feature at the dopant concentrations of Er^{3+} (2 mol%) and Yb^{3+} (20 mol%). The brighter red emission from the current nanostructure compared with those from $NaYF_4:Er^{3+}/Yb^{3+}$ has shown its suitability as an efficient UC luminescence host. It is expected that the achieved intense pure red emission may have potential application in *in vivo* bioimaging.

1. Introduction

In recent years, lanthanide-doped nanoparticles have attracted a great deal of attention due to their unique upconversion (UC) luminescence properties and potential applications in the field of biological fluorescent labels.[1] In comparison with conventional biolabels, such as organic dyes and quantum dots, UC labels have intriguing merits, such as low background light, high penetration depth, high detection sensitivity, and less photo-damage to biological specimens.[2–4] Additionally, low-cost, continuous-wave, near-infrared (NIR) diode lasers, emitting radiation transparent for biomolecules, can be used to efficiently generate visible light, clearly in contrast to the traditional multiphoton labels, which require expensive mode-locked NIR lasers to generate visible light at low efficiency.[5,6] The most efficient UC phosphor currently known is based on Er^{3+} ions in combination with Yb^{3+} ions as sensitizers, which exhibits a green emission (~550 nm) as well as a red emission (~660 nm).[7] Generally, the red region (600–700 nm) and the NIR spectral range (700–1100 nm) are known as the "optical window" of biological tissues due to the minimum absorption in tissues and the

subsequent maximum penetration depth.[8] In contrast, the green emission could not escape from the deep tissue and may also cause many undesired effects that will reduce the imaging sensitivity.[9] Therefore, avoiding the green emission and achieving strong and single-band red emission from the Er^{3+}–Yb^{3+} couple is essential for the deep tissue imaging of fluorescent labels.

Until now, several approaches have been reported to tune the UC emission of the Er^{3+}–Yb^{3+} couple from green/yellow to red.[10–13] It is reported that the relative intensity of red to green in $Y_2O_3:Yb^{3+}/Er^{3+}$ nanocrystals increases gradually with decreasing particle size which is induced by surface effects.[14,15] Moreover, Bai *et al.* has modified the UC luminescence from green to red in Er^{3+}/Yb^{3+} doped zeolites by controlling the Yb^{3+} ion concentration due to the energy back transfer from Er^{3+} to Yb^{3+} ions.[16] Recently, some dopants, such as divalent manganese (Mn^{2+}), have been recognized as effective elements which can decrease the short-wavelength green emission and enhance the long-wavelength red emission because of the energy transfer between Er^{3+} and Mn^{2+} ions.[9] Subsequently, some Mn^{2+}-based nanocrystals have been synthesized to serve as host materials for lanthanide ions. For instance, Wang *et al.* succeeded to prepare Er^{3+}/Yb^{3+} codoped $KMnF_3$ nanocrystals *via* an oil-based synthetic procedure, and realized remarkably pure single-band red emission from the dopant ions.[17] Furthermore, Zhang *et al.* reported ultrasensitive sub-10 nm $NaMnF_3$ nanocrystals codoped with Yb^{3+} and Er^{3+} ions, which show intense pure red UC emission in the presence of Mn^{2+}.[18] However, there are only a few reports on synthetic approaches and UC luminescence

[a]Department of Mechanical Engineering, Iowa State University, Ames, IA 50011, USA. E-mail: nastaran@iastate.edu

[b]Department of Electrical and Electronic Engineering, Graduate School of Engineering, Kobe University, Rokkodai, Nada, Kobe 657-8501, Japan

properties of MnF_2:Er^{3+}/Yb^{3+} nanocrystals, especially with controllable size and morphology.[8] Nanoparticles of different sizes and shapes can be used in many applications including biosensors,[19] drug delivery platforms,[20] and stimuli responsive nanostructures.[21,22,23]

In the present work, we developed a novel strategy to fabricate morphology and size controllable Er^{3+}/Yb^{3+} doped MnF_2 nanostructures. The effects of the ratio between oleic acid and ethanol, and the reaction temperature on the morphology of MnF_2 nanocrystals are systematically investigated. The formation process is elaborated, and the growth mechanism is clarified. We examined the structural and UC luminescence properties of the MnF_2:Er^{3+}/Yb^{3+} nanoclusters as a function of concentrations of dopant Er^{3+}/Yb^{3+} (2–8 : 0–40 mol%).

2. Experimental

2.1. Chemicals and sample preparation

NH_4F (98%), $MnCl_2 \cdot 4H_2O$ (99%), $YbCl_3 \cdot 6H_2O$ (99.9%), $ErCl_3 \cdot 6H_2O$ (99.9%), oleic acid (90%), and absolute ethanol were purchased from Sigma-Aldrich and were used as starting materials without further purification. In a typical synthesis process, MnF_2 doped with 2 mol% Er^{3+} and 20 mol% Yb^{3+} was synthesized as follows: 3.12 mL of 0.2 M $MnCl_2 \cdot 4H_2O$, 0.8 mL of 0.2 M $YbCl_3 \cdot 6H_2O$ and 0.08 mL of 0.2 M $ErCl_3 \cdot 6H_2O$, and 4 mL of 0.6 M NH_4F were added to a beaker containing the mixture of oleic acid (OA) and ethanol (ET) under vigorous stirring. The total amount of oleic acid and ethanol was fixed to 24 mL, and the OA/ET ratio was varied between 0 : 24 mL, 4 : 20 mL, 8 : 16 mL, 12 : 12 mL, 16 : 8 mL, 20 : 4 mL, and 24 : 0 mL according to the experiment requirements. After mixing for 10 min, the resulting mixture was transferred to a 40 mL Teflon-lined autoclave, sealed and heated at 110–200 °C for 12 h. The final products were collected by means of centrifugation, washed with ethanol and deionized water several times to remove any possible remnants, and then dried in a vacuum at 60 °C for 10 h to obtain the dried powders.

2.2. Characterization

The crystal structure of prepared products was analyzed with an X-ray powder diffractometer (Rigaku-TTR/S2) using Cu Kα radiation (λ = 1.54056 Å). The size and morphology of the products were examined by using a field emission scanning electron microscope (FE-SEM, JSM-6700F at an acceleration voltage of 5 kV) equipped with an energy dispersive X-ray spectroscope (EDX, Horiba 7593-H model). The UC luminescence spectra were recorded using a fluorescence spectrophotometer (Horiba Jobin Yvon FluoroLog3) in conjunction with a 980 nm laser as the excitation source. All measurements were performed at room temperature.

3. Results and discussion

3.1. Characterization of the structure and morphology

Fig. 1a presents the XRD patterns of MnF_2 nanostructures synthesized with different OA/ET volume ratios at the reaction
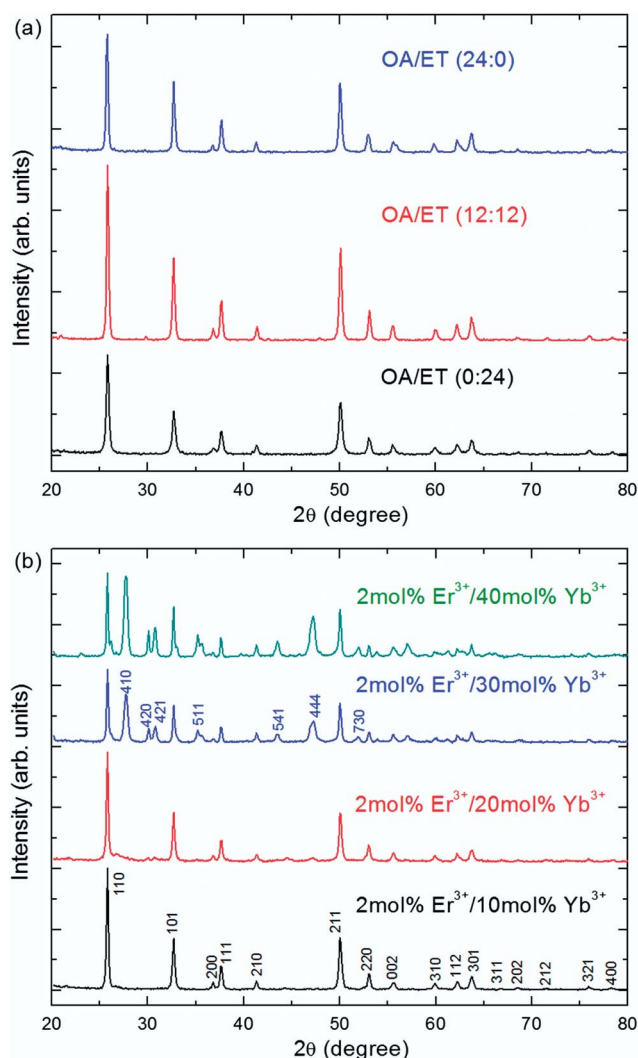
Fig. 1 (a) XRD patterns of MnF_2 nanostructures synthesized with different OA/ET volume ratios at the reaction temperature of 140 °C. (b) XRD patterns of MnF_2 nanostructures (OA/ET = 1) doped with 2 mol% Er^{3+} and (10–40) Yb^{3+} ions.

temperature of 140 °C. It can be seen that all the diffraction peaks of the samples correspond to the tetragonal MnF_2 crystal (JCPDS standard card no. 24-727). The similar diffraction patterns of all samples reveal that the changing of the OA/ET volume ratio does not change the phase. The sharp and strong peaks of MnF_2 crystals suggest high crystallinity of the obtained samples. It is also confirmed that the crystal structure remains constant in the reaction temperature range of 110–200 °C (not shown here). The XRD patterns of MnF_2:2 mol% Er^{3+},(10–40) mol% Yb^{3+} phosphors are also shown in Fig. 1b. It is evidenced that the crystal structure remains the same until the Yb^{3+} concentration reaches 20 mol%, indicating that doped elements have been effectively doped into the host lattice. It is notable that an impurity phase is developed when the Yb^{3+} concentration is above 30 mol%, which can be assigned to the $NH_4Yb_2F_7$ crystal (JCPDS standard card no. 43-0845).

To investigate the morphology and size of obtained samples by changing the experimental parameters, MnF_2 nanocrystals

fabricated with various OA/ET volume ratios are characterized by SEM. As shown in Fig. 2a, with the solvent of ethanol, the irregularly shaped and partially aggregated nanoparticles with sizes around 50–100 nm can be obtained. When 4 mL of oleic acid is added to the solvent, the particle size is decreased to around 20–30 nm, and the formation trend of nanoclusters is shown in Fig. 2b. With the addition of oleic acid (8–12 mL) to the solvent, uniform and well-dispersed products are observed, and the mean diameter is estimated to be around 500 nm (Fig. 2c and d). In particular in the high resolution SEM image, the formation of nanoclusters is confirmed, which consist of

many small nanoparticles in the side-to-side manner (Fig. 2c and d). In the solvent with 16 mL oleic acid, irregularly shaped nanostructures with a large size distribution are observed (Fig. 2e). When the volume of oleic acid is in the range of 20–24 mL, monodispersed lantern-like nanostructures with the average diameter of 400 nm can be obtained (Fig. 2f and g).

Reaction temperature is also an important factor for the growth of nanocrystals, which can influence the reaction rate of crystal formation and further determine the phase and morphology of the final products.[24,25] To evaluate the effect of reaction temperature on the formation of MnF_2 nanoclusters, the samples are fabricated in the temperature range of 110–200 °C. Typical SEM images of the products are shown in Fig. S1a–c,† from which it becomes obvious that the size of MnF_2 is greatly influenced by the reaction temperature. A low reaction temperature results in small MnF_2 nanoclusters, and *vice versa*. The relationship between the particle size and the reaction temperature is illustrated in Fig. S1d.† With the increase of reaction temperature from 110 to 200 °C, the particle size linearly increases from 200 nm to 1.5 μm.

To evaluate the effect of impurity doping on the morphology of MnF_2 nanocrystals, the SEM images of MnF_2:2 mol% Er^{3+},(10–40) mol% Yb^{3+} phosphors are displayed in Fig. 3. It is revealed that the morphology remains similar until the Yb^{3+} concentration reaches 20 mol%, and higher Yb^{3+} doping (≥30 mol%) results in the formation of nanoparticles with the size of 100 nm. Based on the XRD and SEM results of MnF_2:Er^{3+}/Yb^{3+} nanocrystals, doping Yb^{3+} ions at concentrations lower than 20 mol% is essential to preserve the single-phase and morphology of the present host materials.

3.2.   Formation mechanism of MnF_2 nanostructures

To better understand the formation process and growth mechanism of these unusual MnF_2 nanocrystals, the
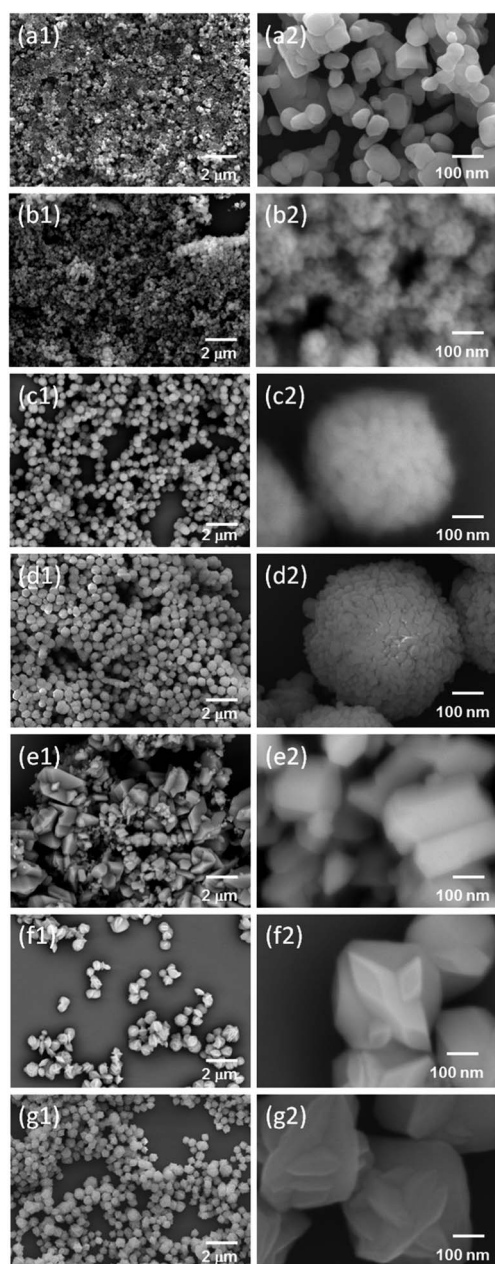
Fig. 2 Low-resolution and high-resolution SEM images of MnF_2 nanocrystals synthesized by various volume ratios of oleic acid to ethanol: (a) 0 : 24 mL; (b) 4 : 20 mL; (c) 8 : 16 mL; (d) 12 : 12 mL; (e) 16 : 8 mL; (f) 20 : 4 mL; (g) 24 : 0 mL.
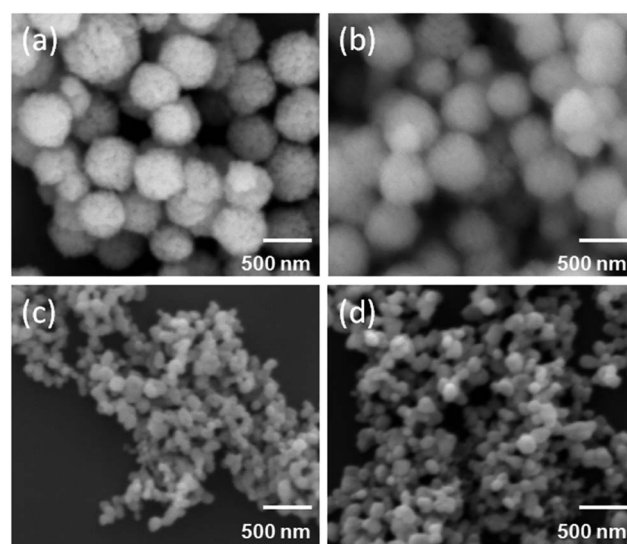
Fig. 3   SEM images of MnF_2 nanoclusters (OA/ET = 1) doped with 2 mol% Er^{3+} and Yb^{3+} of (a) 10 mol%; (b) 20 mol%; (c) 30 mol%, and (d) 40 mol%.

intermediate products collected at different reaction durations were investigated by SEM. Fig. S2a–c† show the morphological evolution of MnF_2 nanoclusters with the reaction time. The product collected after reaction for 1 h mainly exists as nanoparticles with the mean size of 30 nm (Fig. S2a†). With the increase in reaction time to 3 h, the partial nanoparticles are assembled side by side into a sphere shape (Fig. S2b†). After reacting for 12 h, the nanoparticles completely disappeared and only the nanocluster assemblies are observed (Fig. S2c†). Clearly, the sphere-like MnF_2 nanoclusters are formed *via* the self-assembly of the primary nanoparticles and the subsequent iso-oriented fusion in 3D directions. Similarly, the nanolanterns also can be evolved from the nanoparticles *via* the intermediate state (Fig. S2d–f†). It explicitly demonstrates that the growth of MnF_2 nanolanterns follows the Ostwald ripening process.[26] Based on the experimental observations (Fig. S2†), we propose the formation mechanism of MnF_2 nanostructures, which is displayed in Scheme 1. First, the reaction and nucleation of Mn^{2+} and F^- ions can occur during high temperature reaction, which leads to the formation of MnF_2 nanoparticles. Then, these nanoparticles tend to aggregate, driven by the minimization of interfacial energy. When the OA/ET ratio is lower than 0.2, the morphology does not change, and only aggregated MnF_2 nanoparticles are obtained. In the OA/ET ratio range of 0.5–1, well-dispersed sphere-like MnF_2 nanoclusters could be obtained by the self-assembly of the nanoparticles. When the OA/ET ratio is higher than 5, the nanoparticles are developed into nanolanterns *via* Ostwald ripening.

Generally, the growth process of crystals can be separated into two steps, an initial nucleating stage and a subsequent crystal growth process.[27] It has been revealed that the similar initial nucleating states are seen in all shapes, and the amount of oleic acid in the reaction solution plays a very important role in the subsequent crystal growth process. Oleic acid is a commonly used solvent for various nanomaterial fabrications, which can serve as a passivating ligand that prevents the nanocrystals from agglomeration.[28] It is considered that the carboxyl acid group of oleic acid would be adsorbed on MnF_2 nanoparticles and reduce the interactions between these nanoparticles.[29] In the present system, with the moderate amount of oleic acid (8–12 mL), the MnF_2 nanoparticles are self-assembled

into nanoclusters driven by the reduction of the total surface energy, and the oleic acid molecules stabilize the nanoclusters against further aggregation. On the other hand, Ostwald ripening is often found in water-in-oil emulsions where oil molecules diffuse through the aqueous phase and join larger oil droplets.[30] The high concentration of oleic acid (20–24 mL) causes emulsion instability, and the unstable MnF_2 nanoparticles shrink into the solution over time, which will redeposit on the larger particles. Thus small MnF_2 nanoparticles decrease in size until they disappear and large nanolanterns grow even larger.

3.3. Upconversion luminescence properties

Fig. 4a shows the UC emission spectra of MnF_2 nanoclusters doped with various concentrations of Er^{3+} ions. Upon excitation at 980 nm, three UC fluorescence bands at 524 nm, 545 nm, and 656 nm are detected for the MnF_2:8 mol% Er^{3+} sample, which are assigned to the $^2H_{11/2} \rightarrow {}^4I_{15/2}$, $^4S_{3/2} \rightarrow {}^4I_{15/2}$, and $^4F_{9/2} \rightarrow {}^4I_{15/2}$ transitions of Er^{3+} ions, respectively. It is shown that the MnF_2 nanoclusters with lower Er^{3+} concentrations radiate single red UC emission, and the green emission bands disappear. The single-band UC emission can be ascribed to nonradiative energy transfer from the $^2H_{11/2}$ and $^4S_{3/2}$ levels of Er^{3+} to the $^4T_1$ level of Mn^{2+}, followed by back-energy transfer to the $^4F_{9/2}$ level of Er^{3+} (Fig. 4b). The complete disappearance of green emissions of lower Er^{3+} concentration samples suggests an extremely efficient exchange-energy transfer process between the Er^{3+} and Mn^{2+} ions, which is mainly attributed to the close proximity and excellent overlap of energy levels of the Er^{3+} and Mn^{2+} ions in the host lattices.[9,18] For the high Er^{3+} concentration sample, partial Er^{3+} ions may isolate from the host lattices, which is typically observed when divalent host ions are substituted for trivalent lanthanide ions at high concentrations.[17] The isolation effect obstructs the effective energy transfer process between Er^{3+} and Mn^{2+} ions, which results in the observation of green emission bands. It is also noted that the red emission intensity gradually decreases with the increase of Er^{3+} concentration due to the concentration quenching between neighboring Er^{3+} ions (Fig. S3a†).

It is well known that Yb^{3+} ions is an ideal sensitizer for Er^{3+} ions, because of their simple energy state and efficient absorption of 980 nm excitation ($^2F_{7/2} \rightarrow {}^2F_{5/2}$).[31,32] Er^{3+} ions can be first excited to the $^4I_{11/2}$ state through an energy transfer process from Yb^{3+} ions, and then further jump to the $^4F_{7/2}$ state by absorbing the energy from another Yb^{3+} ion (Fig. 4b). The UC luminescence properties are further studied by the addition of Yb^{3+} ions to MnF_2:Er^{3+} nanoclusters, which are displayed in Fig. 4c. Significantly, the single-band feature of the MnF_2:Er^{3+}/Yb^{3+} nanocrystals is well maintained in all Yb^{3+} doped samples. Meanwhile, the strongest red emission appears for the Yb^{3+} (20 mol%) sample which is enhanced by 16 times than the sample without Yb^{3+}, and a further increase of doping concentration leads to the quenching of red emission (Fig. S3b†). Taken together, these comparative studies suggest that our MnF_2:Er^{3+}/Yb^{3+} nanocrystals fabricated by the present synthetic procedure have the strongest single-band emission feature at the dopant concentrations of Er^{3+} (2 mol%) and Yb^{3+} (20 mol%).
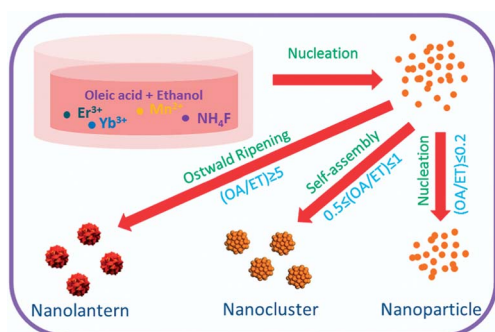
Scheme 1 Schematic illustration of the growth process of MnF_2 nanostructures.

This journal is © The Royal Society of Chemistry 2014

J. Mater. Chem. C, 2014, **2**, 1736–1741 | **1739**
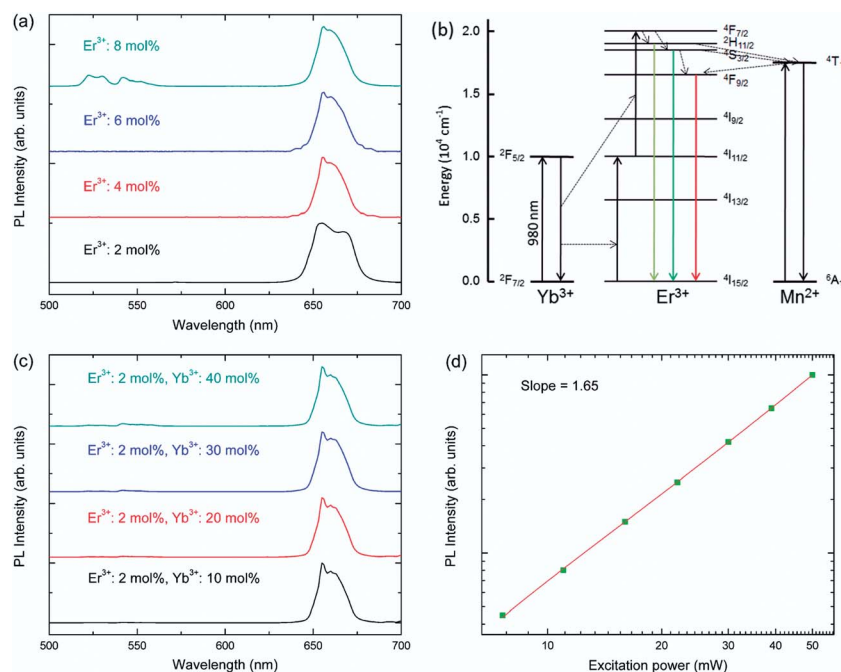
Fig. 4 (a) Upconversion luminescence spectra of MnF_2 nanoclusters doped with different Er^{3+} ion concentrations in the range of 2−8 mol%. (b) Simplified energy level diagrams of Er^{3+}, Yb^{3+} and Mn^{2+} ions and possible transition pathways in MnF_2. (c) Upconversion luminescence spectra of MnF_2 doped with 2 mol% Er^{3+} and 10−40 mol% Yb^{3+} ions. (d) Log−log plots of the red emission intensity *versus* excitation power in 2 mol% Er^{3+}/ 20 mol% Yb^{3+} doped MnF_2 nanoclusters.

To further investigate the UC mechanism, the intensity of red emission in 2 mol% Er^{3+}/20 mol% Yb^{3+} doped MnF_2 nanoclusters is recorded as a function of the 980 nm excitation intensity in log–log plots. As in the UC process, it is well known that the UC emission intensity (I) is relative to the excitation power (P) according to the power law $I \propto P^n$, where n is the number of pump photons absorbed per upconverted photon emitted.[33,34] Fig. 4d indicates that in the MnF_2:2 mol% Er^{3+},20 mol% Yb^{3+} sample, the slope n value of 1.65 is obtained for the red emission band, indicating that two-photon processes are responsible for generating the UC emissions in the present sample.

Fig. 5 Comparison of upconversion luminescence spectra of cubic-phase $NaYF_4$ and MnF_2 host nanocrystals doped with 2 mol% Er^{3+} and 20 mol% Yb^{3+} ions, respectively.

Cubic-phase $NaYF_4$ is recognized as one of the most efficient hosts for performing NIR-to-visible photon conversion due to its low phonon energy and high refractive index, which has been prepared according to the literature (the SEM image is shown in Fig. S4†) and compared with the present Er^{3+}/Yb^{3+} doped MnF_2 UC phosphors.[35,36] Fig. 5 shows the UC luminescence spectra of $NaYF_4$ and MnF_2 doped with 2 mol% Er^{3+} and 20 mol% Yb^{3+} ions, respectively. Under the 980 nm excitation, the $NaYF_4$ sample shows mixture emissions of green and red, though pure red emission is detected from the MnF_2 sample. Despite the emission difference, the red emission intensity of MnF_2:Er^{3+}/ Yb^{3+} is two times stronger and overall (green-plus-red) emissions are 1.4 times greater than those of the $NaYF_4$:Er^{3+}/Yb^{3+} sample, indicating that MnF_2 is a promising host material for deep tissue bioimaging. Such a red-emission enhancement should mostly arise from the efficient cross-relaxation of energy between Mn^{2+} and Er^{3+} ions.

4. Conclusions

In conclusion, we have described a facile synthetic method for the preparation of MnF_2 nanocrystals with Er^{3+} and Yb^{3+} ions homogeneously incorporated into the host lattice. Various morphologies, such as nanoparticles, nanoclusters and nanolanterns, can be obtained with controllable sizes from 200 nm to 1.5 μm. It is revealed that the addition of oleic acid plays an important role in the formation of MnF_2 nanostructures. Doping with Yb^{3+} ions with a concentration lower than 20 mol% is essential to preserve the single phase and morphology of the

1740 | *J. Mater. Chem. C*, 2014, **2**, 1736–1741

This journal is © The Royal Society of Chemistry 2014

MnF_2 host materials. As a result of efficient energy transfer between the dopant Er^{3+} ion and the host Mn^{2+} ion, remarkably pure single-band UC emissions were generated in the red spectral region. The strongest red emission in these Er^{3+}/Yb^{3+} doped nanocrystals has been realized at the dopant concentrations of Er^{3+} of 2 mol% and Yb^{3+} of 20 mol%. The achieved red emission is two times stronger and overall (green-plus-red) emissions are 1.4 times greater than those of $NaYF_4$:Er^{3+}/Yb^{3+} nanocrystals. The excellent optical properties make these interesting nano-structures promising for application in *in vivo* bioimaging.

Acknowledgements

References

1 W. Q. Zou, C. Visser, J. A. Maduro, M. S. Pshenichnikov and J. C. Hummelen, *Nat. Photonics*, 2012, **6**, 560.

2 X. F. Yu, M. Li, M. Y. Xie, L. D. Chen, Y. Li and Q. Q. Wang, *Nano Res.*, 2010, **3**, 51.

3 G. Tian, Z. J. Gu, X. X. Liu, L. J. Zhou, W. Y. Yin, L. Yan, S. Jin, W. L. Ren, G. M. Xing, S. J. Li and Y. L. Zhao, *J. Phys. Chem. C*, 2011, **115**, 23790.

4 X. J. Xie and X. G. Liu, *Nat. Mater.*, 2012, **11**, 842.

5 N. J. J. Johnson, A. Korinek, C. H. Dong and F. C. J. M. van Veggel, *J. Am. Chem. Soc.*, 2012, **134**, 11068.

6 W. Y. Yin, L. N. Zhao, L. J. Zhou, Z. J. Gu, X. X. Liu, G. Tian, S. Jin, L. Yan, W. L. Ren, G. M. Xing and Y. L. Zhao, *Chem. – Eur. J.*, 2012, **18**, 9239.

7 E. M. Chan, G. Han, J. D. Goldberg, D. J. Gargas, A. D. Ostrowski, P. J. Schuck, B. E. Cohen and D. J. Milliron, *Nano Lett.*, 2012, **12**, 3839.

8 M. Y. Xie, X. N. Peng, X. F. Fu, J. J. Zhang, G. L. Lia and X. F. Yu, *Scr. Mater.*, 2009, **60**, 190.

9 G. Tian, Z. J. Gu, L. J. Zhou, W. Y. Yin, X. X. Liu, L. Yan, S. Jin, W. L. Ren, G. M. Xing, S. J. Li and Y. L. Zhao, *Adv. Mater.*, 2012, **24**, 1226.

10 F. Wang, R. R. Deng, J. Wang, Q. X. Wang, Y. Han, H. M. Zhu, X. Y. Chen and X. G. Liu, *Nat. Mater.*, 2011, **10**, 968.

11 D. Q. Chen, L. Lei, R. Zhang, A. P. Yang, J. Xu and Y. S. Wang, *Chem. Commun.*, 2012, **48**, 10630.

12 J. Zhou, Z. Liu and F. Y. Li, *Chem. Soc. Rev.*, 2012, **41**, 1323.

13 L. J. Zhou, Z. J. Gu, X. X. Liu, W. Y. Yin, G. Tian, L. Yan, S. Jin, W. L. Ren, G. M. Xing, W. Li, X. L. Chang, Z. B. Hu and Y. L. Zhao, *J. Mater. Chem.*, 2012, **22**, 966.

14 J. A. Capobianco, F. Vetrone, J. C. Boyer, A. Speghini and M. Bettinelli, *J. Phys. Chem. B*, 2002, **106**, 1181.

15 X. Bai, H. W. Song, G. H. Pan, Y. Q. Lei, T. Wang, X. G. Ren, S. Z. Lu, B. Dong, Q. L. Dai and L. Fan, *J. Phys. Chem. C*, 2007, **111**, 13611.

16 Z. H. Bai, M. Fujii, K. Imakita and S. Hayashi, *Microporous Mesoporous Mater.*, 2013, **173**, 43.

17 J. Wang, F. Wang, C. Wang, Z. Liu and X. G. Liu, *Angew. Chem., Int. Ed.*, 2011, **50**, 10369.

18 Y. Zhang, J. D. Lin, V. Vijayaragavan, K. K. Bhakoo and T. T. Y. Tan, *Chem. Commun.*, 2012, **48**, 10322.

19 I. H. El-Sayed, X. Huang and M. A. El-Sayed, *Nano Lett.*, 2005, **5**, 829.

20 P. Ghosh, G. Han, M. De, C. K. Kim and V. M. Rotello, *Adv. Drug Delivery Rev.*, 2008, **60**, 1307.

21 R. Montazami, S. Liu, Y. Liu, D. Wang, Q. Zhang and J. R. Heflin, *J. Appl. Phys.*, 2011, **109**, 104301.

22 R. Montazami, C. M. Spillmann, J. Naciri and B. R. Ratna, *Sens. Actuators, A*, 2012, **178**, 175.

23 S. Liu, R. Montazami, Y. Liu, V. Jain, M. Lin, X. Zhou, J. R. Heflin and Q. M. Zhang, *Sens. Actuators, A*, 2010, **157**, 267.

24 Z. H. Bai, M. Fujii, T. Hasegawa, K. Imakita, Y. Miwa, M. Mizuhata and S. Hayashi, *Microporous Mesoporous Mater.*, 2011, **145**, 21.

25 J. M. Ma, J. Teo, L. Mei, Z. Y. Zhong, Q. H. Li, T. H. Wang, X. C. Duan, J. B. Lian and W. J. Zheng, *J. Mater. Chem.*, 2012, **22**, 11694.

26 J. H. Yao, K. R. Elder, H. Guo and M. Grant, *Phys. Rev. B: Condens. Matter Mater. Phys.*, 1993, **47**, 14110.

27 X. C. Duan, X. D. Liu, Q. Chen, H. B. Li, J. Li, X. Hu, Y. Y. Li, J. M. Ma and W. J. Zheng, *Dalton Trans.*, 2011, **40**, 1924.

28 L. Zhang, R. He and H. C. Gu, *Appl. Surf. Sci.*, 2006, **253**, 2611.

29 K. Sakai, N. Umemoto, W. Matsuda, Y. Takamatsu, M. Matsumoto, H. Sakai and M. Abe, *J. Oleo Sci.*, 2011, **60**, 411.

30 Y. Chang, J. J. Teo and H. C. Zeng, *Langmuir*, 2005, **21**, 1074.

31 J. C. Boyer, L. A. Cuccia and J. A. Capobianco, *Nano Lett.*, 2007, **7**, 847.

32 H. X. Mai, Y. W. Zhang, R. Si, Z. G. Yan, L. D. Sun, L. P. You and C. H. Yan, *J. Am. Chem. Soc.*, 2006, **128**, 6426.

33 H. T. Sun, L. L. Hu, C. L. Yu, G. Zhou, Z. C. Duan, J. J. Zhang and Z. H. Jiang, *Chem. Phys. Lett.*, 2005, **408**, 179.

34 H. T. Sun, C. L. Yu, Z. C. Duan, L. Wen, J. J. Zhang, L. L. Hu and S. X. Dai, *Opt. Mater.*, 2006, **28**, 448.

35 G. S. Yi, H. C. Lu, S. Y. Zhao, G. Yue, W. J. Yang, D. P. Chen and L. H. Guo, *Nano Lett.*, 2004, **4**, 2191.

36 G. Y. Chen, H. C. Liu, G. Somesfalean, H. J. Liang and Z. G. Zhang, *Nanotechnology*, 2009, **20**, 385704.

This journal is © The Royal Society of Chemistry 2014

J. Mater. Chem. C, 2014, **2**, 1736–1741 | **1741**